Thermal Conductivity Temperature Dependence of Water Confined in Nanoporous Silicon

Xiaorui Wang, William Gonçalves, David Lacroix, Mykola Isaiev, Séverine. Gomès, Konstantinos Termentzidis

To cite this version:

Xiaorui Wang, William Gonçalves, David Lacroix, Mykola Isaiev, Séverine. Gomès, et al.. Thermal Conductivity Temperature Dependence of Water Confined in Nanoporous Silicon. Journal of Physics: Condensed Matter, 2022, 10.1088/1361-648X/ac664b . hal-03691014

HAL Id: hal-03691014
https://hal.science/hal-03691014

Submitted on 8 Jun 2022

Thermal Conductivity Temperature Dependence of Water Confined in Nanoporous Silicon

Xiaorui WANG
Univ. Lyon, INSA-Lyon, CETHIL CNRS-UMR5008, F-69621, Villeurbanne, France

William GONÇALVES
Univ. Lyon, INSA-Lyon, CETHIL CNRS-UMR5008, F-69621, Villeurbanne, France

David LACROIX
Université de Lorraine, CNRS, LEMTA, Nancy F-54000, France

Mykola ISAIEV
Université de Lorraine, CNRS, LEMTA, Nancy F-54000, France

Séverine GOMÈS
Univ. Lyon, INSA-Lyon, CETHIL CNRS-UMR5008, F-69621, Villeurbanne, France

Konstantinos TERMENTZIDIS
Univ. Lyon, INSA-Lyon, CETHIL CNRS-UMR5008, F-69621, Villeurbanne, France
E-mail: `konstantinos.termentzidis@insa-lyon.fr`

February 2020

Abstract.

Recently, it has been shown that high density nanoconfined water was the reason of the important enhancement of the effective thermal conductivity up to a factor of 50% of a nanoporous silicon filled with water. In this work, using Molecular Dynamics simulations, we further investigate the role of the temperature T (from 285 to 360 K) on the thermal conductivity enhancement of nanohybrid porous silicon and water system. Furthermore, by studying and analysing several structural and dynamical parameters of the nanoconfined water, we give physical insights of the observed phenomena. Upon increasing the temperature of the system, the thermal conductivity of the hybrid system increases reaching a maximum for T= 300 K. With this article, we prove the existence of new heat flux channels between a solid matrix and a nanoconfined liquid, with clear signatures both in the radial distribution function, mean square displacements, water molecules orientation, hydrogen bond networks and phonon density of states.

Keywords: Molecular Dynamics, Heat Transfer, Porous Silicon, Nanoconfined Water, Solid/liquid Interface, Hydrogen Bond Networks

1. Introduction

Liquids can modify the thermal properties of composite materials and could be used to tune the effective thermal conductivity of solid porous matrices due to their different thermal properties, their viscosity and their phase transition properties, etc [1, 2, 3, 4]. Solid-liquid hybrid composites could be a new strategy to obtain easily tailored physical properties. With the revolution of the nanofabrication methods and the functionalization of the solid surface techniques [5, 6, 7], solid-liquid hybrid nanocomposites have started to be used in various industrial applications such as high density microelectronic [8], thermoelectric [9, 10, 11], photo-electronic devices [12, 13], etc. Furthermore, a wide variety of solid-liquid hybrid composites can be elaborated today, including all the materials presenting a solid-liquid mixture at the nanoscale; for instance nanofluids (colloidal suspension of solid nanoparticles) [14], or nanostructured solid matrix with filled liquids [15]. In this regard, understanding physical mechanisms in these solid/liquid hybrid systems is a critical issue for both fundamental research and technological issues.

A number of studies showed an enhancement of the effective thermal conductivity of nanocomposites [16, 17]. Experimentally, Lishchuk et al. [18] used Photo Thermal (PT) technique to show that the thermal conductivity of a nanoporous silicon filled with oil is twice the one of the dry sample. A similar behavior has been observed by Wang et al. [19] using Time Domain Thermoreflectance (TDTR) on a Al_2O_3/water nanofluid. On the other hand J.A.Thomas [20] found that the fully diffusive thermal conductivity of water-filled carbon nanotubes (CNTs) is 20%-35% lower than that of empty CNTs. The reduction of the thermal conductivity of the latter system could be due to the large vibrational mismatch of the CNTs with the water, which leads to much higher thermal resistance, also known as Kapitza resistance [21, 22] and the initially high thermal conductivity of the dry CNTs. For both cases, enhancement or suppression of the effective thermal conductivity of hybrid (solid/liquid) nanocomposites, it seems that the effect of a liquid, often water on the thermal conductivity can not be predicted by effective macroscopic modeling [23]. The effective thermal conductivity of a solid-liquid nanoporous composites can be influenced by various factors such as porosity, size and spatial distribution of pores and the thermal boundary resistance [24, 25].

For dry nanoporous silicon, Fang et al. [26] demonstrated that the thermal conductivity of the material is strongly affected by the porosity and the pore surface area. J.-H. Lee et al. [27] found values for the thermal conductivity of nanoporous silicon two orders of magnitude smaller than the bulk depending on the pore diameter and the spacing between pores. When there is an amorphous shell around the pores one can obtain sub-amorphous thermal conductivity [28]. Concerning wet nanoporous samples, the impact of water filling on the thermal conductivity is not yet well understood. In a recent study [23], the thermal conductivity of the water filled nanoporous silicon has been strongly impacted by the stratification of the liquid close to the solid surface and the total liquid-solid interfacial area. The physical mechanisms behind the important enhancement of the effective thermal conductivity of such systems, probably due to the dense water film (density of 1.4 g/cm^3), are not yet fully identified.

In the present paper, we investigate the structural and dynamical properties of the confined water to understand the variations of the thermal conductivity of wet nanoporous silicon as a function of the system's temperature. Molecular Dynamics (MD) simulations are used to model the hybrid composites and to appraise the effective thermal conductivity. This paper is organised into five sections. After the introduction, the simulation method is presented, i.e., the interaction parameters and MD simulation settings are described in details. Then, in the results section we investigate the impact of temperature (from 285 to 360 K) on the thermal conductivity of the wet nanoporous silicon. Structural and dynamical properties of water such as radial distribution functions, diffusion coefficient, hydrogen bond network analysis and phonon density of states are compared between the core and the near-interface confined water.

2. Modeling and simulation methodology

All MD simulations here are conducted using the open source code Large-scale Atomic/ Molecular Massively Parallel Simulator (LAMMPS) [29, 30]. The effective thermal conductivity is computed using Equilibrium Molecular Dynamics (EMD) methodology. In the following subsections, details about the simulation methods are provided. The temperatures of T_{eq}= 285, 300, 315, 330, 345 and 360 K are investigated here keeping constant the initial density of water of 1 g.cm^{-3}.

2.1. Interatomic potential

The interactions between silicon atoms are defined using the original Stillinger-Weber (SW) potential [31]. The expression of SW is presented in the supplementary materials. All interatomic parameters used in this study are displayed in Table 1. The thermal conductivity of bulk silicon, at room temperature, has been successfully calculated via this potential [32]. The water model used for this study is the Extended Simple Point Charge (SPC/E) [33], which is considered to be a good compromise between reliability [34] and computation time. The interactions between hydrogen and silicon atoms are neglected. The interactions only between silicon and oxygen atoms are modeled using a Lennard-Jones potential (LJ) in Eq.1 [35], which is sufficient and physically meaningful for many relevant applications [17, 36]:

$$U(r_{ij}) = 4\varepsilon \left[\left(\frac{\sigma}{r_{ij}} \right)^{12} - \left(\frac{\sigma}{r_{ij}} \right)^{6} \right] \qquad (1)$$

where ε is the depth of the LJ potential, σ is the finite distance at which the inter-particle LJ potential is null, and r_{ij} is the distance between atoms i and j. Considering

Table 1: Interatomic potential parameters of Stillinger-Weber (SW) [31] and Lennard-Jones (LJ) [39] used in the molecular dynamics simulation. The parameters without units are dimensionless.

	ε(eV)	σ (Å)	**a**	λ	γ	
Si-Si-Si	2.1683	2.0951	1.80	21.0	1.20	
	$\cos\theta$	**A**	**B**	**p**	**q**	**tol**
	-0.3333	7.0496	0.6022	4.0	0.0	0.0

	ε_{ij}(kcal/mol)	σ_{ij} (Å)	$\mathbf{q_{ii}}(e)$	$\mathbf{d_{ij}}$ (Å)	$\theta_{\mathbf{iji}}(^\circ)$
O-H	0	0		1.0	109.47
O-O	0.1553	3.166	-0.8476		
H-H	0	0	0.4238		
Si-O	0.3632	2.6305	0		

the contact angle 87.5° of water droplet on the silicon surface [37], the LJ value for Si-O are chosen as: $\varepsilon_{Si-O} = 15.75$ meV and $\sigma_{Si-O} = 2.6305$ Å. The cut-off distance beyond which the interatomic potential vanishes has been chosen to be 2.5 σ. The bonds and angles of the water molecules are constrained during the simulation using the SHAKE algorithm [38].

2.2. Modeling the studied configurations

All the configurations studied here are simulated using periodic boundary conditions. First, bulk crystalline silicon box with dimensions of $8a_0 \times 8a_0 \times 8a_0$ ($a_0 = 5.43$) has been generated, which corresponds to a cubic sample of the size length $L = 43.4$ Å. The porosity of the studied system is set to 15.5%, which is reached by removing a sphere of atoms within a radius of $R = 14.48$ Å from the simulation box center. Then, a spherical volume "crystalline-like" water with a lattice constant of a_0^w is set in the pore. The initial density of water is 1 g/cm^3 with the $a_0^w = 3.1$ Å.

The atom velocities are initialized using a Maxwell- Boltzmann distribution, relaxing the system in the NVT ensemble for 200 ps at the temperature T_{eq}. Then, a NVE run during 70 ns is realised to calculate the thermal conductivity using EMD method (see Sec.2.4 for more details). Fig.1 provides the simulated configurations: initial dry nanoporous crystalline silicon, addition of the crystalline water spherical nanoinclusion inside the pore and then in (c) the hybrid system after equilibrium. The snapshots are produced using the visualization software OVITO [40].

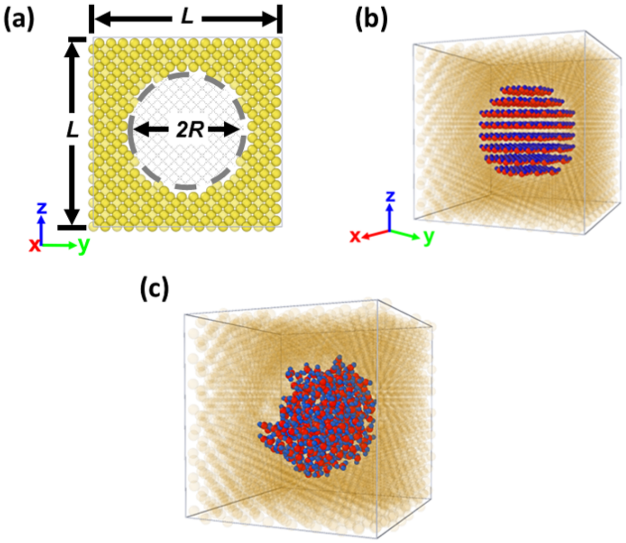

Figure 1: The simulation models : (a) Cross-section of the dry nanoporous silicon with unit cell dimensions $8a_0 \times 8a_0 \times 8a_0$, (b) initial and (c) after equilibrium configuration of the hybrid system (water and silicon) with water filling the pores.

2.3. Structural and dynamical characterization of system

The water density profile as a function of distance from the pore center has been calculated and depicted in Fig. 2. To detail enough the picture of the physical properties of the water molecules at the interface, we have divided the whole porous volume into 100 spatial spherical bins with the same center of the pore. The local thermal properties can be impacted by the bin size choice, especially when they are of the order of the lattice constant [41]. Here, we have chosen a bin thickness of 0.2172 Å. The same bin size has been used previously and it could describe correctly the thermal fluctuations both at the liquid and at the solid/liquid interface [23]. Size effect tests have been performed to avoid artifacts. As it has been observed previously in the literature [42, 23], two peaks in the liquid density profile are well observed near the solid/liquid interface before reaching a plateau with constant density. According to the density profile, we will separate the nanoconfined water into two regions. The first one is the core that includes all the water molecules within a distance of 9 Å from the center of the pore, and the second one is the shell which corresponds to the region from the edge of the core to the edge of pore (from 9 to 14.48 Å in Fig. 2) in which we observe fluctuations of the density (two maxima of the density close to the solid surface). The fluctuation of the density observed in the center of the pore are related to our choice to have equal thickness bins instead of equal volume bins. This is the reason of the density variations in the center of the pore, which we neglect. The importance here is the density profile close to the solid surface which does not depend on the choice of the bin size. The structural and dynamical properties

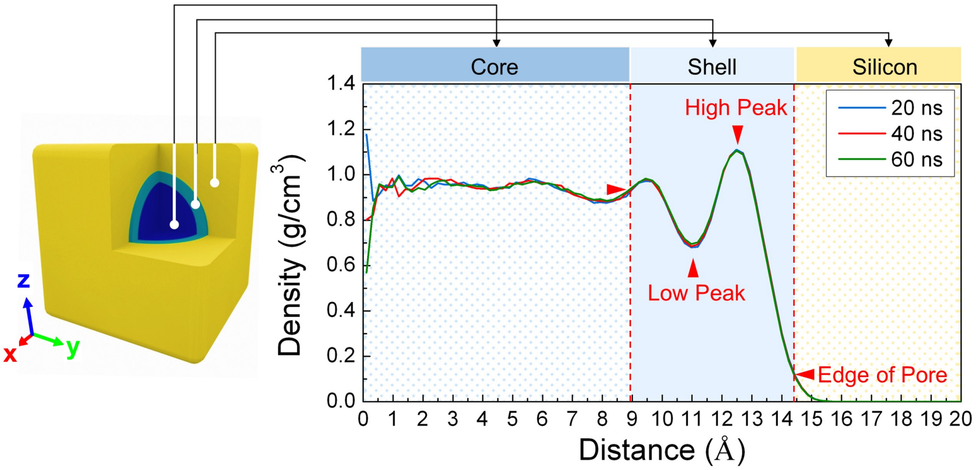

Figure 2: Density profiles of water nanoporous silicon system at 300 K, averaged every 20 ns. The core and shell of the nanoconfined water are defined and marked in the figure.

of water will be compared between these two regions.

The Radial Distribution Functions (RDFs), the diffusion coefficient and the angle orientation of the nanoconfined water are also been studied in details to obtain physical insights of the interactions between the nanoconfined water and the porous matrix. The diffusion coefficient is calculated from the Mean Square Displacement (MSD) of the atoms using the Einstein relation [43]:

$$D = \lim_{t\to\infty} \frac{1}{2Nt} < |r(t'+t) - r(t')|^2 > \tag{2}$$

where r is the position of the atom of a water molecule at time t and D is the diffusion coefficient. The orientation of the water molecules is measured by computing the angle, θ, between the radial direction of the oxygen atom (determined from the oxygen atom and the pore center coordinates) and the molecular dipole moment from the same water molecule.

Other structural and topological analysis properties are extracted using the *ChemNetworks* software package [44]: eg. the hydrogen bond networks, which can be observed as sub-structure inside the water phase [44]. The number of hydrogen bonds and the geodesic length of the network have been computed to further characterize the nanoconfined water. As suggested by Ozkanlar et al. [44], a H-bond is defined by the distance r_{O-H} of H and O atoms from two different molecules within a distance of 2.5 Å and a O-H-O angle ϕ between 145° and 185°, as shown in Fig.3. The number of hydrogen bonds is counted under this criteria within the cutoff distance 10 Å. Also under this criteria, there is a shortest continuous pathway connecting any two water molecules. The geodesic distance, labeled as gd [44], is defined as the number of hydrogen bonds passing through this pathway. We keep the same criterion for the water in the core and the

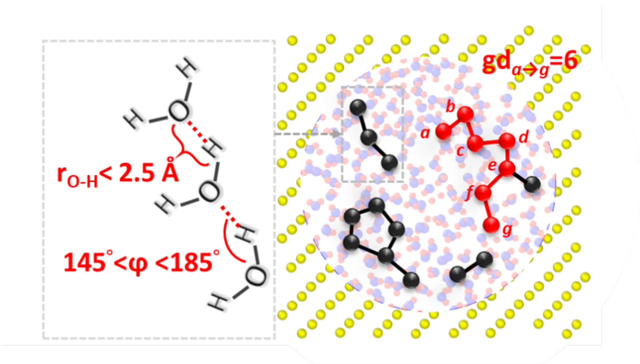

Figure 3: Definition of the intermolecular hydrogen bonds for water (left) and the illustration of geodesic length (right) between two water molecules. In the right subfigure the molecules of water are depicted in a simple sphere, to simplify the picture. The geodesic length for the red chain of spheres is 6.

shell area, as it has already been used for a water system under different temperatures and densities in previous works [45].

2.4. Calculation of the effective thermal conductivity

To calculate the effective thermal conductivity of the system, Equilibrium Molecular Dynamics (EMD) simulations are performed. The thermal conductivity tensor is computed using the Green-Kubo [46, 47] formula:

$$\mathbf{k} = \frac{1}{3k_BVT^2}\int_0^\infty < J(0)J(t) > dt \tag{3}$$

where J denotes the microscopic heat current given by

$$J(t) = \sum_{i=1}^{N}\sum_{j=1,j\neq i}^{N}[\frac{1}{2}r_{ij}\cdot(F_{ij}\cdot\nu_i) \quad + \frac{1}{6}\sum_{k=1,k\neq i,j}(r_{ij}+r_{jk})\times(F_{ijk}\cdot\nu_i)] \tag{4}$$

V is the volume of the particle, T is the equilibrium temperature, k_B is the Boltzmann constant, r_{ij} is given by $r_{ij} = |r_i - r_j|$. F_{ij} and F_{ijk} are the two and three-body forces, respectively.

Using EMD simulations, a long run is necessary to obtain a convergence of the thermal conductivity, here the time interval between 45 and 70 ns has been used to calculate the thermal conductivity via the Green-Kubo formula (see supplementary materials-B). For each configuration/temperature six simulations with different initial conditions have been performed to reduce the uncertainty of the obtained results.

2.5. Density of states

The vibrational density of states (VDOS) are obtained with the Fourier transform of the velocity auto-relation function (VACF) [48]. When the system is in the equilibrium and within the NVE ensemble, a temporal average of the velocity auto-correlation function (VACF) for a specific group of atoms (water molecules or silicon porous matrix here) every 0.01 ps during 0.5 ns has been directly extracted from LAMMPS (using the compute vacf command). Then, the Fourier Transform is applied to VACF, and the results are smoothed filtering by Savitzky-Golay filter [49]. This statistical method provides better performances for long-time simulation of large systems [50].

3. Results and discussions

3.1. Effective thermal conductivity as a function of the temperature

The thermal conductivities of the hybrid solid-liquid as well as the dry nanoporous silicon system are depicted in Fig.4 within the temperature range: 285 K to 360 K. For comparison, the thermal conductivity with EMA model is estimated with the Eq.5. In addition, the thermal conductivities of bulk water calculated here and from experimental data [51] are plotted for the same temperature range in Fig.4.

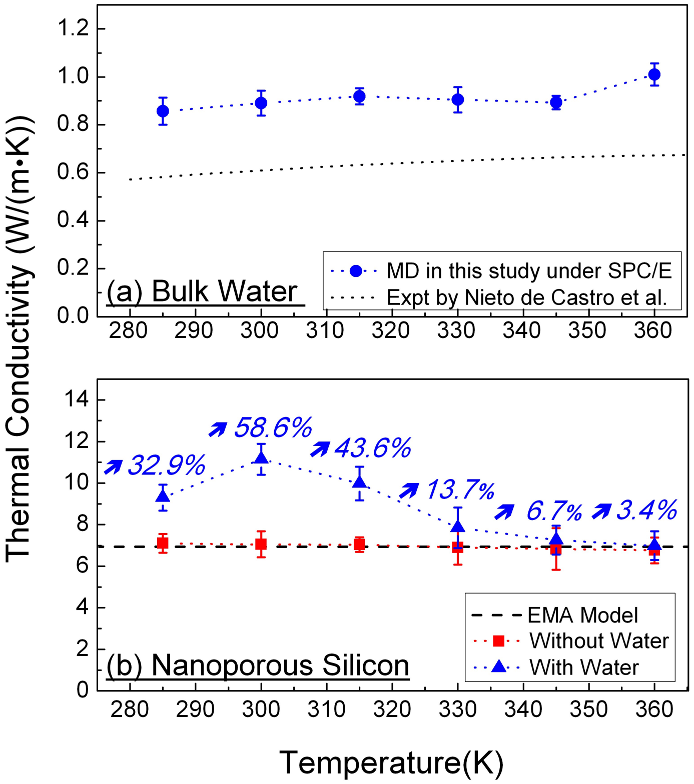

Figure 4: Thermal Conductivity as a function of the temperature of (a) bulk water both experimental (dotted line) [52] and simulated (blue spheres) and (b) dry (red squares) and wet (blue triangles) nanoporous silicon with 15.51% porosity. Finally the effective thermal conductivity calculated with the EMA approach with the Eq. 5 is depicted with dashed black line.

The thermal conductivity of bulk water both calculated and measured experimentally slightly increases with the temperature. The difference of about 20% between the simulated and experimental values depends on the used model and it is comparable to previous reported values, shown in Table 2. For example, the thermal conductivity of the bulk water simulated in this study with the SPC/E model is 0.87 ± 0.051 W/(mK) at 300 K, while the experimental value is about 0.61 W/(mK) at the room temperature (298 K) [51, 53, 54]. It can be seen in the Table 2 that our results are in a good agreement with previous reported values (0.808 W/(mK)) using the same model [55]. The correlation with the temperature has been also observed previously in other liquid systems, such as methanol [56], ethylene glycol or oil [57]. This tendency can be explained by the fact that the water expands in increasing the temperature, making the molecules to move more freely, thus enabling to transfer heat more efficiently.

Concerning results for the dry and wet nanoporous silicon, we observed in the sub-Fig.4(b) that the thermal conductivity of the dry nanoporous silicon almost remains constant varying the temperature, with average value of 6.9 ± 0.11 W/(mK), while the effective thermal conductivity of the wet nanoporous silicon system first increases with the temperature reaching a maximum at 300 K, and then decreases and saturates at the same value as the dry system for temperatures greater than 345 K. This unexploited till now behavior is the central point of our study. To understand the origin of this phenomenon, and based on the known thermal conductivity of the bulk solid matrix and the bulk liquid water, we have first used the well-known Effective Media Approach (EMA) numerical model to calculate the effective thermal conductivity k_{eff}^{EMA} of the hybrid composite. We note here, that for the macroscopic scale, the EMA is considered as a reliable approach [58]. The general expression of k_{eff}^{EMA} in this study is deduced from ref. [59] as:

$$k_{eff}^{EMA} = k_{Si}^{matrix} \frac{k_{H_2O}^{bulk}(1+2\alpha) + 2k_{Si}^{matrix} + 2f_v[k_{H_2O}^{bulk}(1-\alpha) - k_{Si}^{matrix}]}{k_{H_2O}^{bulk}(1+2\alpha) + 2k_{Si}^{matrix} - f_v[k_{H_2O}^{bulk}(1-\alpha) - k_{Si}^{matrix}]} \tag{5}$$

where k_{Si}^{matrix} and $k_{H_2O}^{bulk}$ are the TC of the matrix crystalline silicon and bulk water, f_v is the porosity of system, while α is a dimensionless parameter defined, which takes into the thermal contact resistance account, as:

$$\alpha = R_K^{Si/H_2O} k_{Si}^{matrix}/r \tag{6}$$

here the r is the nano-inclusion radius and R_K^{Si/H_2O} is the Interfacial Thermal Resistance (ITR) (or Kapitza resistance) between silicon and water. In the Eq.5, we used $k_{H_2O}^{bulk}$ the calculated value here. k_{Si}^{matrix} is taken as 8.83 W/(mK) from the previous study [23] with respect of Minnich and Chen model [60]. The R_K^{Si/H_2O} is calculated as 6.8×10^{-8} Km^2/W by the Kapitza length in Ref [61].

Results for the EMA are shown in Fig.4(b) by the black dashed line. The effective thermal conductivity of the wet nanoporous silicon calculated by EMA is constant

Table 2: Summary of the thermal conductivity of different water models SPC/E, TIP3P, TIP4P, TIP4P/2005, TIP5P calculated with MD simulations for temperatures around the ambient one and extracted from several references.

Model	$T(K)$	$\mathbf{k}_{MD}(W/(m \cdot K))$	Ref.
SPC/E	298	0.93 ± 0.016	[62]
TIP3P	298	0.88 ± 0.019	[62]
TIP3P	298	0.608	[63]
TIP4P	298	0.82 ± 0.015	[62]
TIP4P/2005	298	0.91 ± 0.014	[62]
TIP5P	298	0.68 ± 0.007	[62]
SPC/E	300	0.87 ± 0.051	This study
SPC/E	300	0.808 ± 0.038	[55]
TIP4P	300	0.641	[64]
SPC/E	315	0.92 ± 0.032	This study
TIP4P/2005	324	0.85	[65]
SPC/E	325	0.87	[65]

around 7 W/(mK) in the studied temperature range. Thus, we can conclude that the macroscopic theories and models cannot apply well in the case of hybrid nanocomposite.

Going back to the results in Fig.4, the thermal conductivity of the wet nanoporous silicon at the temperature window of 285 K to 300 K increases from 9.30 to maximum value of 11.18 W/(mK). The maximum enhancement of the thermal conductivity due to the nanoconfined water is of the order of 58% and as mentioned above this is observed at 300 K. The enhancement of the effective thermal conductivity for nanoporous silicon with water is obviously induced by the presence of the water. What is striking is the maximum of the effective thermal conductivity around 300 K, which initiate the question, why there is a decrease of the thermal conductivity after 300 K. This might be related to the enhancement of the boundary scattering after this temperature or to an eventual phase transition of water inside the pore. Concerning the overall enhancement of the thermal conductivity, a previous thorough study [23] at 300 K has demonstrated that the significant enhancement of the thermal conductivity of the porous silicon liquid composite compared to the dry porous system, is due to the liquid density fluctuation close to solid-liquid interface as "layering effect".

3.2. Density profiles

To understand the particular thermal conductivity results and specially the maximum at 300 K, several interfacial structural properties of confined water are analysed. We start with the density profiles of the nanoconfined water from the center to the edge of the pore. This quantity is calculated and depicted for several temperatures in Fig.5.

The density at the core of the water (central part from 0 to about 9 Å) fluctuates around 1 g/cm^3. Then in the transition region (from about 9 Å to 13.6 Å), and we observe a couple of maxima and minima of the water density. This phenomenon has been already observed at solid-liquid interfaces at the atomic scale [66]. We stress the attention to the fact that increasing the temperature there is a smoothing of the low peak maximum and minimum localised at 5.5 and 8 Å from the center of the pore, thus reduction of distance from the solid surface in which a stratification of water molecules is observed. For large distance which is greater than the radius of pore (14.48 Å), the water density vanishes to zero revealing that some water molecules penetrate in the silicon matrix through the edge of the pore. In the density profiles we observe also that the depth of the minimum decreases in increasing the temperature, something that it is expected view the increase of the thermal agitation of the molecules in increasing the temperature. To depict in more clear way the dependence of the density peaks with the temperature, both the maximum and minimum values of the density peaks as well as the water shell thickness are plotted in Fig. 6. Upon the temperature increases, the high peak value of the density changes slightly, but the low peak shows an increasing trend.

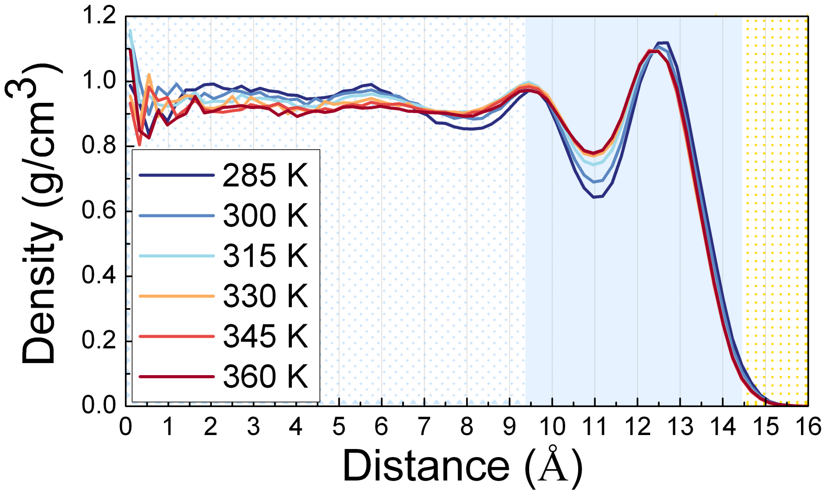

Figure 5: Density profiles of hybrid water-nanoporous silicon system along the radial direction from the center of the pore towards the edge of the pore under different temperatures. All profiles are obtained by averaging over 50 ns of simulations.

3.3. Radial distribution functions

The RDFs of the bulk water as well as the nanoconfined water have been studied also here to check for eventual phase transition of the nanoconfined water close to the solid surface. The radial distribution functions g(r) of bulk water, and water in the core and shell for two different temperatures (300, 360 K) are depicted in Fig.7. We

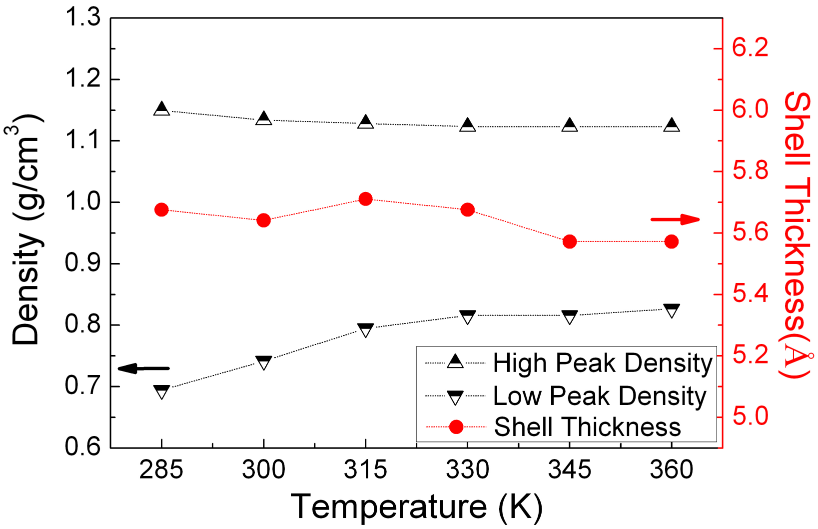

Figure 6: The shell thickness and density values of high and low peaks as a function of temperature.

observe that the position of the first neighbor peak does not change significantly for the core and shell water molecules compared to the bulk water and it seems that it is independent of temperature. We notice also here that nanoconfined liquids do not attend the value of 1 as it is expected for bulk liquids and this has already been observed previously [67, 68]. What one can easily notice is the differences in g(r) between the different temperatures as well as the position of the water inside the pore (core and shell). The higher temperature induces the decrease of the intensity of the RDF peak by 10%-15%. While the temperature impacts only slightly the value of the peak of the maximum of the RDF, the discrepancy gets more important for the shell water molecules compared to the core ones. We observe that the water molecules in the shell group have almost double intensity first peak compared to the molecules characterized here as core. Another important remark here is that the shell water molecules exhibit higher intensity of the RDF compared to the bulk water meaning that there are much more localised and ordered atoms in the shell compared to the bulk water or compared to the core nanoconfined water. This observation persists even at higher temperatures (360 K) but it is less pronounced. At this point we can also comment on the possible phase transition: we do not observe such phase transition. A possible gas would be appeared with a much flatter first peak and then a constant value equal to 1 (no secondary peaks). A possible ice formation is also excluded, as in such case the minimum between the first and second peak approaches to zero. The message from this sub-study is that at 300 K the shell water is much more ordered than the bulk water and the temperature difference impacts much more the shell than the core water atoms. In any case we do not observe a phase transition of the water.

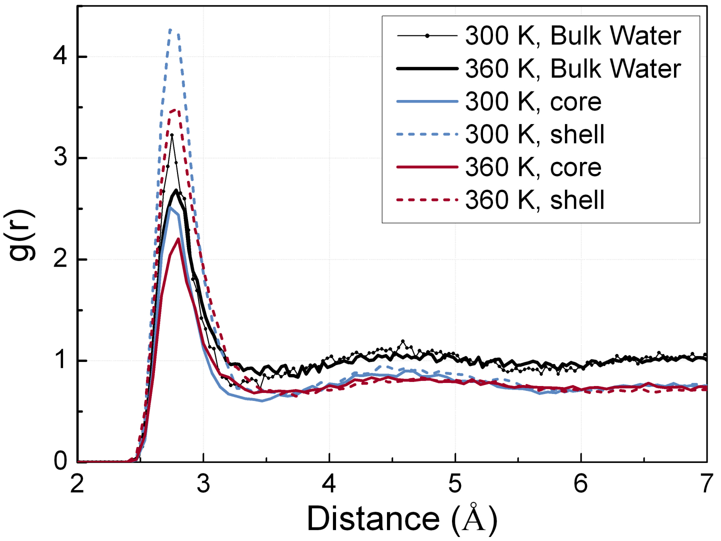

Figure 7: Partial Radial Distribution Functions (RDFs) of O-O pair for different parts (core and shell) of nanoporous silicon hybrid system confined with water under different temperatures. When calculate RDFs, a reference O particle is chosen from the core or shell while the second O atom could belong either to shell or the core atoms. For comparaison the bulk water RDF is depicted for both temperatures considered here.

3.4. Velocity and motion displacement

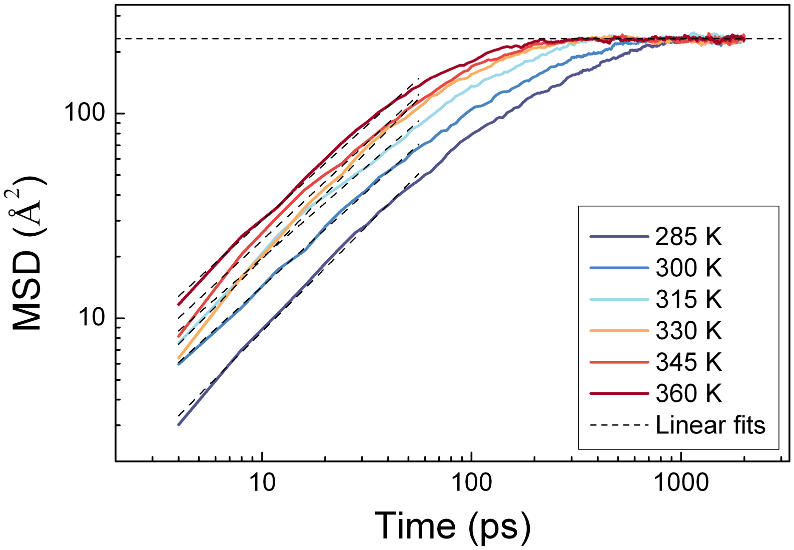

Figure 8: Log-log plot of Mean Square Displacement Function (MSD) of water confined in nanoporous silicon for different temperatures, and the fitted lines within 50 ps.

Table 3: Diffusion coefficient for different temperatures of the nanoconfined water extracted by Fig.8

Temperature (K)	285	300	315	330	345	360
Slope	1.03	0.93	0.89	1.04	0.95	0.93
D (Å^2/ps)	0.20	0.27	0.41	0.29	0.44	0.58

The thermal conductivity of liquids depends beside temperature and pressure, on their nature, the velocity and the relative displacement of the molecules between them and with the solid walls in a sense that in general the enhanced motion of liquid enhances the thermal transport [69, 17]. To check if the molecular motion of the nanoconfined water inside a pore has an impact on the thermal properties, we have studied the mean square displacement (MSD) to estimate the diffusion coefficient. The MSD of confined water in nanoporous silicon is depicted in Fig.8. We observe that the water molecules for different temperatures show the same kind of displacement: the profiles vary approximately linearly before 200 ps, and then the particles exhibit a saturation as the MSD profiles become flat systematically after 1000 ps for all temperatures. Moreover, the plateau of the saturation near 232.1 Å^2 is independent of the temperature. Mosaddeghi [70] also observed a similar plateau for the MSD of the nanoconfined water between two parallel graphite plates with inter-wall distance less than 7 Å.

Vincent Tejedor et al. introduced an anomalous diffusion exponent α, expressed as $MSD = 2NDt^{\alpha}$, for N dimensions [71]. We have calculated the diffusion coefficient from the intercept and the exponent value from the slope of the fitted curve in Fig.8. The diffusion coefficient is reported in Table.3 with the slope of the curves. The value $\alpha = 1$ indicates a classical Brownian motion at the first 100 ps. After that, the slope decreases with the time until about 200 ps, and then stabilizes (slope equal to zero). We think that this is a signature of a non Brownian diffusion, due to the confined geometry. S.Chakraborty [72] found a similar diffusion for a single line of water molecules confined inside a short, open-ended carbon nanotubes. The water molecules move collectively as a single unit due to the presence of strong hydrogen bonding between adjacent water molecules.

In Table.3, the simulated diffusion coefficients of the nanoconfined water in a pore with radius of 14.48 Å is of the order of magnitude of 10^{-9} m^2s^{-1}. The values increase from 0.20 Å^2/ps at 285 K, to 0.58 Å^2/ps at 360 K. Thus, increasing the temperature results on the enhancement of the diffusion coefficient. This trend has also been observed in the case of bulk water, with the value of 0.16 Å^2/ps at 276 K and 0.23 Å^2/ps at 290 K [73]. Making the comparison between the nanoconfined and the bulk water, we see that the temperature impacts much more the diffusion coefficient for the nanoconfined water than the bulk.

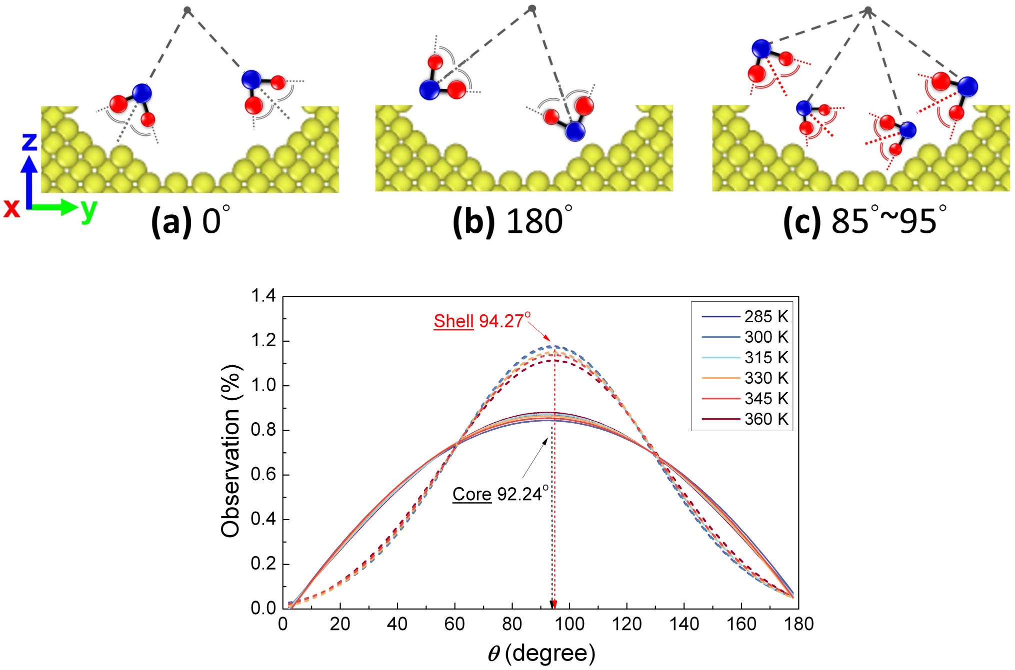

Figure 9: The angle θ is taken as the one between the molecular dipole moment and the radial direction of oxygen atom to the center of the pore for each water molecule, as a function of temperature for both core and shell water molecules and for different temperatures. The most likely angle for the water molecules in the center and shell region, are 92.2° and 94.3°. The curves shown in the figure are smoothed by fitting the Gaussian distribution.

3.5. Water molecule orientation

The presence of hydrogen bond networks allows water to exhibit many unusual properties. The strength, the density and the distribution of H-bonds might have a deep effect on the thermal dissipation. To explore the translational and rotational states of water molecules, in particular for those near the solid/liquid interface, the orientational dynamic is studied under different temperatures and for both the shell and the core atoms (see Fig. 9). The angle distribution follows a Gaussian distribution with mean value of 92.2° for core molecules and a bit shifted 94.3° for the shell molecules. What is evident from the graph is that the distribution of the angles of the shell molecules is much more narrow comparing to the core ones, which reveals that oxygen atoms closer to the solid/liquid interface are less free to spin compared to the inner water molecules. The phenomenon looks independent of the temperature at least for the core molecules, for the shell molecules we can observe a slight decline of the peak in increasing the temperature, which seems rational taking into account that the temperature will increase the thermal agitation.

3.6. Hydrogen bond network

Topological analysis of H-bond networks is calculated using *ChemNetworks* as a post-processing package of *LAMMPS* in our study. Fig.10 shows the number of water molecules connected interacting through the hydrogen bonds as a function of temperature separately in the core, the shell and in the ensemble of them, compared with bulk system for different temperatures, with aim to compare the dynamic behavior of the water molecule networks.

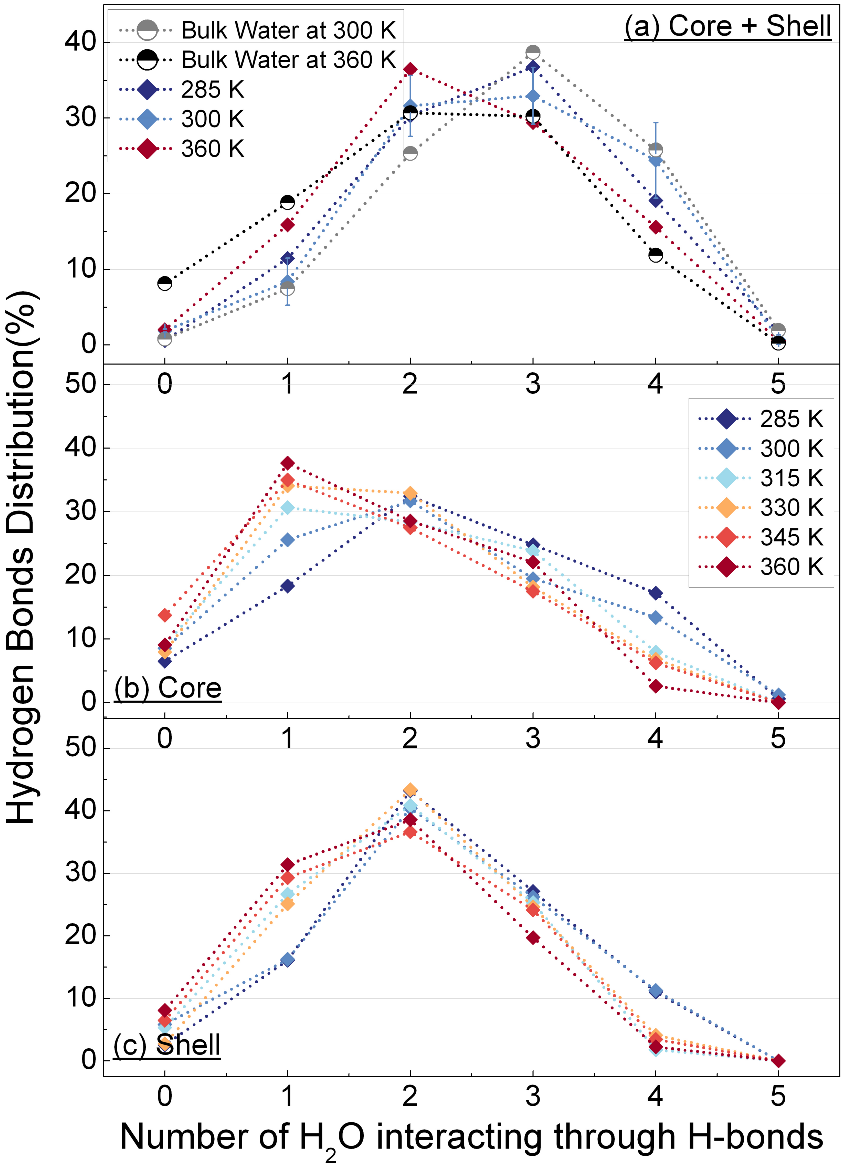

Figure 10: Distribution number of hydrogen bonds between two neighboring water molecules for (a) bulk water and nanoconfined water and for (b and c) separated water molecules shell/core for different temperatures . The interaction length cut-off was set to be 10 Å.

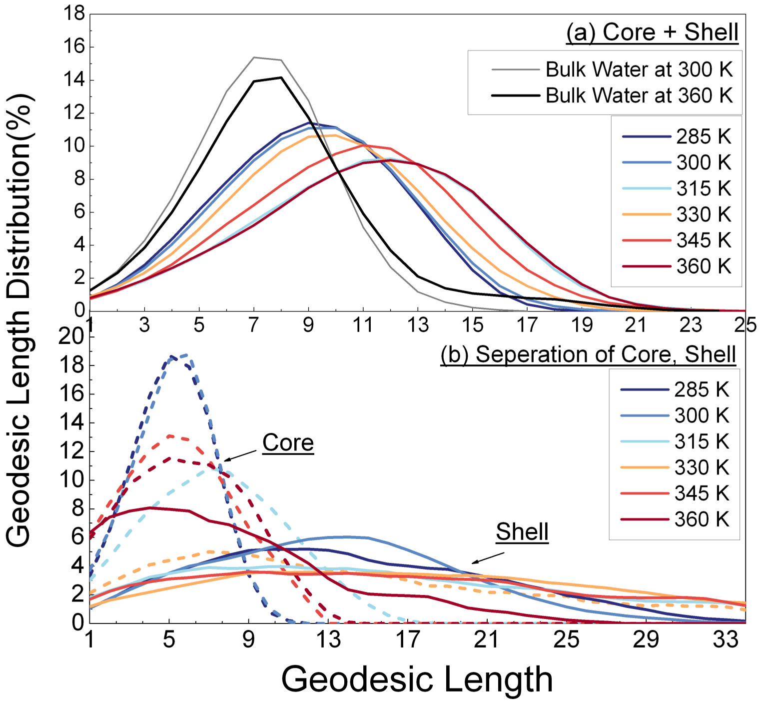

Figure 11: Distribution of geodesic lengths of bulk and nanoconfined water (a), and on the core and shell (b), for different temperatures.

In the top panel we observe that for bulk water the temperature shifts to higher numbers of the interconnected with hydrogen-bonds water molecules, eg. at 300 K there is no zero number of independent water molecules and the majority of networking molecules contains 2, 3 and 4 H-bonds, thus three, four or five water molecules stack together. The distribution of H-bonds for bulk water at 300 K (8% for 1 H-bond, 23% for 2 H-bonds, 38% for 3 H-bonds, 26% for 4 H-bonds and less than 1% for 0 and 5 H-bonds) agrees very well with previous works with SPC/E model [74, 44]. At 360 K, there is a shift to lower numbers of H-bonds and the majority of water molecules creates networks of two, three and four molecules. For the nanoconfined water, the differences between two temperatures (300 and 360 K) is more blurry. Finally, it seems that the temperature has not a systematic effect on the H-bond networks. When we separate the core and shell water molecules, we observe first of all, higher values are distributed for 2 H-bonds for the core. The overall distribution of the number of long hydrogen bonds for the shell is more than the one for the core. More connections of networking in the shell is probably correlated to our remark that the high density water layer close to the solid/liquid interface has potential to cause the higher thermal conductivity of hybrid nanosystems. A second phenomenon observed with these results is that with temperature augment, the water molecules have the tendency to create shorter networks, thus to be more isolated. This observation might be related to the decrease of the effective thermal conductivity of the hybrid nanosystem upon increasing the temperature.

At 300 K, the distributions show less isolated H-bonds and about 5% higher distributions than 285 K (10% higher distributions than 360 K) for 4 bonds. This state is regarded as a ”perfect” network wherein each H_2O has exactly 4 H-bonds, as has been published in prior work [75]. Under this state, the bonded connection is much stronger and remains the longest. Thus, it could be roughly concluded that a probable ”perfect” network is found at 300 K though hydrogen bond networks, meaning that the greater H-bonds distribution value leads to the greater thermal conductivity. Then as temperature increases, the percentage of hydrogen bonds formed with a small number H-bonds increases, which indicates that the distance between the intermolecular hydrogen-oxygen bonds gradually increases and the molecular forces decrease.

The state of connectivity due to the H-bond networks of water is also evaluated by the analysis of the geodesic length distribution (gd), depicted in Fig.11. As observed in Fig.11(a), the gd for the bulk water exhibit Gaussian shape, with a peak of geodesic length of 15 %, and average length of 7 water interconnected molecules. The temperature does not affect considerable the gd of the bulk water. The gd profiles of the nanoconfined water for temperature less than 300 K is a bit shifted compared to the bulk water to higher geodesic lengths, having a quite narrow distribution and centered around the mean value of 9 H-bonds. For temperatures higher of 315 K to 360 K, the distributions become much broader with significant population of geodesic lengths greater than 10 meaning that more contiguous hydrogen bonded paths are promoted. The same tendencies are observed in Fig. 11(b) where we have separated the core and the shell molecules. Overall, the shell water molecules behave more contiguous than the core molecules. More specifically, the core region is smaller than the shell region alone or the core plus shell regions together. The geodesic length depends on the volume of the studied region. This is the reason of the much narrow distribution for the core compare to the shell alone. Concerning the fluctuations, when the core and shell are considered together, the geodesic length exhibits much less fluctuations because it is more favorable to create the hydrogen bond pathways without large variations. This is due to the observation of a collective movement of the water inside the pore during our simulations. The confined water is turning around and touching always the solid surface, thus this impacts the geodesic length when it is considered separately for the core or the shell. Hence, we believe that the distribution fluctuation differences are due to the movement of the ensemble of the water molecules.

3.7. Density of states

Phonon Density of States (DOS) of solid-liquid hybrid system for different temperatures are depicted in Fig.12. The aim of the DOS study is to identify possible heat flow channels through the dense water layer close to the solid surface, which might explain the enhanced thermal conductivity of the hybrid nanosystem.

Let's focus first on the DOS of silicon atoms around the pore, both the dry and wet conditions. First of all we observe no shift of the transverse optical peak of the silicon atoms when water is confined compared to the dry system and secondly a hybridisation of the optical and acoustic longitudinal peaks (merged of the second and third peak compared to the bulk crystalline silicon). The latter has been observed previously on other systems and involves undercoordinated silicon atoms at the surfaces of the pores [76]. Concerning the effect of the confinement on the water DOS compared to the bulk water, we see that there is a softening of the modes, then a decrease of the higher peak which corresponds to the longitudinal peak of silicon, with an important enhancement of the DOS in the lower frequencies which correspond to the transverse phonon silicon peak. What we can conclude from this part is that the modification of the DOS of the hybrid system is in the direction of increasing the overlap area between the DOS of the silicon matrix and the nanoconfined water. Qualitatively this increase of the common surface support the idea that the heat can travel easier between the solid and the liquid as their DOS are modified respectively in a way to create heat flux channels. We notice also that there is an important enhancement of the low frequency DOS of the nanoconfined water, thus a more efficient heat transfer.

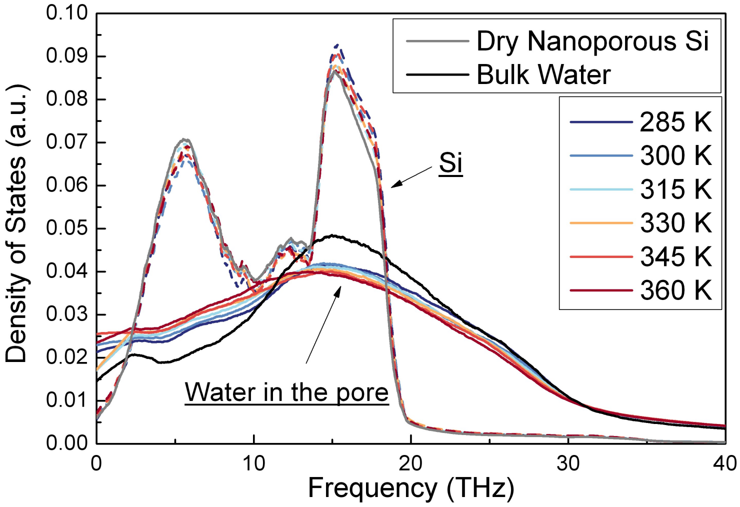

Figure 12: Density of states for bulk water (black continuous line), dry (grey continuous line) and wet nanoporous silicon (pointed lines), as well as nanoconfined water in a pore (continuous lines), for different temperatures.

4. Conclusions

To summarize the current work, the origin of an important enhancement of the effective thermal conductivity of wet nanoporous samples compared to dry ones at room temperature has been studied here. The underlying mechanisms are related to the stratification of the water molecules at the vicinity of the solid/liquid interface.

This enhancement is much more important than the one that can be predicted by using macroscopic effective models. Furthermore, here we observed for the first time a maximum of the thermal conductivity of the solid/liquid nanohybrid system at 300 K, which vanishes for temperatures greater than 345 K. To understand this non-monotonic behavior, several structural and dynamical properties of the nanoconfined water, separated in a core water molecules (bulk-like) and shell water molecules (dense water layer close to the solid/liquid interface) have been studied numerically.

First of all the water molecule density followed a stratification effect close to the solid interface and the water density fluctuations decreased in increasing the temperature. The average value of density of the maximum peak is around 1.15 g/cm^3 and this does not change with the temperature. In contrast, the value of the minimum peak at 285 K is 0.7 g/cm^3 and it increases with the temperature reaching the value of 0.85 g/cm^3 at 360 K. Furthermore, secondary peaks disappear in increasing the temperature. Nevertheless, the density variations cannot be connected to the maximum effective thermal conductivity at 300 K, as this variation is rather monotonic. Then with RDFs analysis, we have more physical insights concerning the maximum of the effective thermal conductivity: at 300 K the shell water is much more ordered than the bulk water and the temperature difference affected much more the shell than the core water atoms.

On the other hand, dynamical features such as the mean square displacement and the diffusion coefficient showed a saturation of movement over a long period of observation. An uncorrelated Brownian motion of nanoconfined water is observed at the beginning of the observation, followed by a confined diffusion. The diffusion coefficient shows that nanoconfined water responds more strongly to the temperature than the bulk water. Concerning the orientation of water molecules, we have observed that oxygen atoms close to the solid/liquid interface are more rigid compared to the inner water molecules, but this phenomenon is independent of temperature. The hydrogen bond networks study for nanoconfined water reveals that the majority of molecules preserves similar networks to the bulk water and that the temperature does not have a systematic effect on the H-bond networks. The overall distribution of the number of long hydrogen bonds for the shell is much more than the one for the core. More connections of networking in the shell might be correlated to our remark that the high density water layer close to the solid/liquid interface has potential to cause the higher thermal conductivity of hybrid nanosystems. This conclusion is also supported by the tendency of water molecules to create shorter networks in increasing the temperature, corresponding to the decrease of the effective thermal conductivity of the hybrid nanosystems upon increasing the temperature. The geodesic length profiles of the nanoconfined water for temperature less than 300 K is a bit shifted compared to the bulk water to higher geodesic lengths, having a quite narrow distribution. For temperatures higher than 315 K, the distributions became much broader, with significant population of geodesic lengths greater than 10. The shell water molecules behaved more contiguous than the core molecules. Last but not the least was that the DOS of the silicon pores atoms and the nanoconfined water molecules increased their juxtaposed areas and this qualitatively means that new heat flux channels are established between the solid matrix and the nanoconfined water, but without explaining the maximum of the thermal conductivity at 300 K.

Supplementary Material

The Stillinger-Weber potential for Silicon

In this work, the original Stillinger-Weber potential is used for the Si-Si interactions, which was proposed by Stilling and Weber [31]. With this potential, the total energy E includes two-body and three-body interactions:

$$\begin{aligned} E &= \sum_{i<j} \Phi_2(i,j) + \sum_{i\neq j, j<k} \Phi_3(i,j,k) \\ &= \sum_{i<j} \varepsilon\phi_2(r_{ij}) + \sum_{i\neq j, j<k} \varepsilon\phi_3(r_{ij}, r_{ik}, \theta_{ijk}) \end{aligned}$$

where ϕ are the function of two- and three-body:

$$\begin{aligned} \phi_2(r_{ij}) \quad &= A[B\left(\frac{\sigma}{r_{ij}}\right)^p - \left(\frac{\sigma}{r_{ij}}\right)^q] \exp\left(\frac{1}{r_{ij}/\sigma - a}\right) \\ \phi_3(r_{ij}, r_{ik}, \theta_{ijk}) &= \lambda\left(cos\theta_{ijk} + \frac{1}{3}\right)^2 \exp\left(\frac{\gamma}{r_{ij}/\sigma - a}\right) \\ &\quad \times \exp\left(\frac{\gamma}{r_{ik}/\sigma - a}\right) \end{aligned}$$

Time evolution of the thermal conductivity

The thermal conductivity has been extracted after sufficient time to obtain satisfactory convergence, usually after 45 ns. The correlation length has been set to 2 ps and the time interval for dump is 40 ps, which has already proved to be long enough to obtain converged values [77]. A fit is performed on the blue shade part of the data in this figure to obtain the final value of thermal conductivity.

Acknowledgments

This work was funded by the China Scholar Council (CSC) and partially by the French National Research Agency (ANR) project "Hotline" ANR-19-CE09-0003. We are also thankful to GENCI-IDRIS for providing computational resources with the grant 2020-A0080911395.

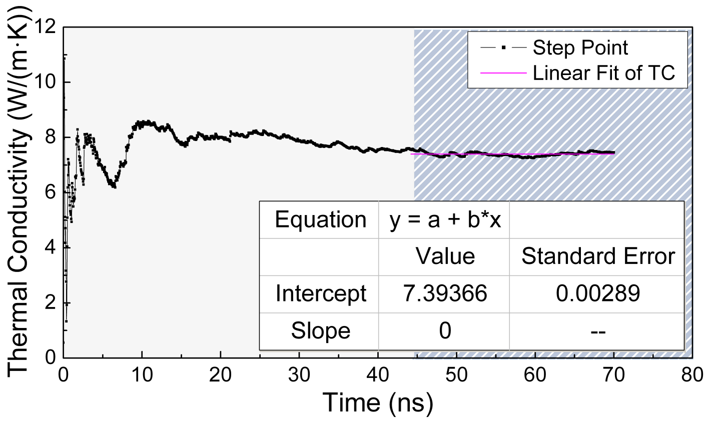

Equation	y = a + b*x	
	Value	Standard Error
Intercept	7.39366	0.00289
Slope	0	--

Figure 13: Time evolution of the thermal conductivity of nanoporous silicon system confined with water at 300 K. The total duration of EMD simulation is 70 ns, while only the last 20 ns are used to estimate the thermal conductivity.

References

[1] Mala G M, Li D and Dale J 1997 International Journal of Heat and Mass Transfer **40** 3079–3088

[2] Brovchenko I, Geiger A and Oleinikova A 2004 Journal of Physics: Condensed Matter **16** S5345

[3] Hanks D F, Lu Z, Sircar J, Salamon T R, Antao D S, Bagnall K R, Barabadi B and Wang E N 2018 Microsystems & nanoengineering **4** 1–10

[4] Gao H, Wang J, Chen X, Wang G, Huang X, Li A and Dong W 2018 Nano Energy **53** 769–797

[5] Gin D L 1997 Functionalized nanoporous polymer membranes with well-defined pore architectures via lyotropic liquid-crystalline monomers. Tech. rep. CALIFORNIA UNIV BERKELEY DEPT OF CHEMISTRY

[6] Piraux L, Dubois S, Duvail J, Radulescu A, Demoustier-Champagne S, Ferain E and Legras R 1999 Journal of materials research **14** 3042–3050

[7] Sheng Z, Ding Y, Li G, Fu C, Hou Y, Lyu J, Zhang K and Zhang X 2021 Advanced Materials 2104851

[8] Han H, Mérabia S and Müller-Plathe F 2017 The journal of physical chemistry letters **8** 1946–1951

[9] Yanagi K, Kanda S, Oshima Y, Kitamura Y, Kawai H, Yamamoto T, Takenobu T, Nakai Y and Maniwa Y 2014 Nano letters **14** 6437–6442

[10] Dai D, Zhou Y and Liu J 2011 Renewable Energy **36** 3530–3536

[11] Zhao K, Qiu P, Shi X and Chen L 2020 Advanced Functional Materials **30** 1903867

[12] Heske C, Groh U, Fuchs O, Weinhardt L, Umbach E, Schedel-Niedrig T, Fischer C H, Lux-Steiner M C, Zweigart S, Niesen T et al. 2003 The Journal of chemical physics **119** 10467–10470

[13] Volokh M, Peng G, Barrio J and Shalom M 2019 Angewandte Chemie International Edition **58** 6138–6151

[14] Kio M T E 2014

[15] Ong Z Y and Pop E 2010 Physical Review B **81** 155408

[16] Sachdeva P and Kumar R 2009 Applied Physics Letters **95** 223105

[17] Sachdeva P 2009

[18] Lishchuk P, Andrusenko D, Isaiev M, Lysenko V and Burbelo R 2015 International Journal of Thermophysics **36** 2428–2433

[19] Wang X, Zhou M, Xu W, Zhang Z and Sun F 2018 Thermal conductivity measurements of Al_2O_3/water nanofluids using time-domain thermoreflectance method and hot wire method International Heat Transfer Conference Digital Library (Begel House Inc.)

[20] Thomas J A, Iutzi R M and McGaughey A J 2010 Physical Review B **81** 045413
[21] Kapitza P 1941 J. Phys.(Moscow) **4** 181
[22] Huxtable S T, Cahill D G, Shenogin S, Xue L, Ozisik R, Barone P, Usrey M, Strano M S, Siddons G, Shim M et al. 2003 Nature materials **2** 731–734
[23] Isaiev M, Wang X, Termentzidis K and Lacroix D 2020 Applied Physics Letters **117** 033701
[24] Vo T Q and Kim B 2015 International Journal of Precision Engineering and Manufacturing **16** 1341–1346
[25] Yenigun O and Barisik M 2019 International Journal of Heat and Mass Transfer **134** 634–640
[26] Fang J and Pilon L 2011 Journal of Applied Physics **110** 064305
[27] Lee J H, Grossman J, Reed J and Galli G 2007 Applied Physics Letters **91** 223110
[28] Verdier M, Termentzidis K and Lacroix D 2016 Journal of Applied Physics **119** 175104
[29] Plimpton S 1995 Journal of computational physics **117** 1–19
[30] All M 1995 J. Comput. Phys **117**
[31] Stillinger F H and Weber T A 1985 Physical review B **31** 5262
[32] Dong H, Fan Z, Shi L, Harju A and Ala-Nissila T 2018 Physical Review B **97** 094305
[33] Mark P and Nilsson L 2001 The Journal of Physical Chemistry A **105** 9954–9960
[34] Orsi M 2014 Molecular Physics **112** 1566–1576
[35] Lennard-Jones J E 1924 Proc. Roy. Soc. A **106** 463–477
[36] Ozcelik H G, Sozen Y, Sahin H and Barisik M 2020 Applied Surface Science **504** 144359
[37] Isaiev M, Burian S, Bulavin L, Gradeck M, Lemoine F and Termentzidis K 2016 Molecular Simulation **42** 910–915
[38] Ryckaert J P, Ciccotti G and Berendsen H J 1977 Journal of computational physics **23** 327–341
[39] Horn H W, Swope W C, Pitera J W, Madura J D, Dick T J, Hura G L and Head-Gordon T 2004 The Journal of chemical physics **120** 9665–9678
[40] Stukowski A 2009 Modelling and Simulation in Materials Science and Engineering **18** 015012
[41] Vo T Q, Barisik M and Kim B 2016 The Journal of chemical physics **144** 194707
[42] Isaiev M, Burian S, Bulavin L, Chaze W, Gradeck M, Castanet G, Merabia S, Keblinski P and Termentzidis K 2018 The Journal of Physical Chemistry B **122** 3176–3183
[43] Allen M 1987 Dj tildesley computer simulation of liquids
[44] Ozkanlar A and Clark A E 2014 Journal of computational chemistry **35** 495–505
[45] Bakó I, Lábas A, Hermansson K, Bencsura Á and Oláh J 2017 Journal of Molecular Liquids **245** 140–146
[46] Che J, Cagin T and Goddard III W A 2000 Nanotechnology **11** 65
[47] Baroni S, Bertossa R, Ercole L, Grasselli F and Marcolongo A 2020 Handbook of Materials Modeling: Applications: Current and Emerging Materials 809–844
[48] Owens E T and Daniels K E 2013 Soft Matter **9** 1214–1219
[49] Press W H and Teukolsky S A 1990 Computers in Physics **4** 669–672
[50] Desmarchelier P, Termentzidis K and Tanguy A 2020 Semiconductor Science and Technology **35** 094001
[51] Nieto de Castro C, Li S, Nagashima A, Trengove R and Wakeham W 1986 Journal of physical and chemical reference data **15** 1073–1086
[52] Ramires M L, Nieto de Castro C A, Nagasaka Y, Nagashima A, Assael M J and Wakeham W A 1995 Journal of Physical and Chemical Reference Data **24** 1377–1381
[53] Abdulagatov I and Azizov N 2005 International journal of thermophysics **26** 593–635
[54] Huber M L, Perkins R A, Friend D G, Sengers J V, Assael M J, Metaxa I N, Miyagawa K, Hellmann R and Vogel E 2012 Journal of Physical and Chemical Reference Data **41** 033102
[55] Zhao Z, Sun C and Zhou R 2020 International Journal of Heat and Mass Transfer **152** 119502
[56] Guevara-Carrion G, Nieto-Draghi C, Vrabec J and Hasse H 2008 The Journal of Physical Chemistry B **112** 16664–16674
[57] Keblinski P, Eastman J A and Cahill D G 2005 Materials today **8** 36–44
[58] Hui P, Zhang X, Markworth A and Stroud D 1999 Journal of materials science **34** 5497–5503

[59] Nan C W, Birringer R, Clarke D R and Gleiter H 1997 Journal of Applied Physics **81** 6692–6699
[60] Minnich A and Chen G 2007 Applied Physics Letters **91** 073105
[61] Pham A T, Barisik M and Kim B 2014 International journal of precision engineering and manufacturing **15** 323–329
[62] Mao Y and Zhang Y 2012 Chemical Physics Letters **542** 37–41
[63] Sedighi M and Mohebbi A 2014 Journal of Molecular Liquids **197** 14–22
[64] Lee S H and Kim J 2019 Molecular Physics **117** 1926–1933
[65] Römer F, Lervik A and Bresme F 2012 The Journal of chemical physics **137** 074503
[66] Yu T, Bai L, Xu Z and Yang X 2018 Molecular Simulation **44** 1–10
[67] Giovambattista N, Rossky P J and Debenedetti P G 2006 Physical Review E **73** 041604
[68] Da Silva L B 2014 Journal of Nanostructure in Chemistry **4** 104
[69] Ju S P and Yang C C 2018 Computational Materials Science **154** 256–265
[70] Mosaddeghi H, Alavi S, Kowsari M and Najafi B 2012 The Journal of chemical physics **137** 184703
[71] Tejedor V, Bénichou O, Voituriez R, Jungmann R, Simmel F, Selhuber-Unkel C, Oddershede L B and Metzler R 2010 Biophysical journal **98** 1364–1372
[72] Chakraborty S, Kumar H, Dasgupta C and Maiti P K 2017 Accounts of chemical research **50** 2139–2146
[73] Qvist J, Schober H and Halle B 2011 The Journal of chemical physics **134** 144508
[74] Wang C H, Bai P, Siepmann J I and Clark A E 2014 The Journal of Physical Chemistry C **118** 19723–19732
[75] Speedy R J, Madura J D and Jorgensen W L 1987 Journal of Physical Chemistry **91** 909–913
[76] Verdier M, Han Y, Lacroix D, Chapuis P O and Termentzidis K 2018 Journal of Physics: Materials **2** 015002
[77] Alosious S, Kannam S K, Sathian S P and Todd B 2021 Langmuir **37** 2355–2361